Scripta Materialia 162 (2019) 472–476

Contents lists available at ScienceDirect

Scripta Materialia

journal homepage: www.elsevier.com/locate/scriptamat

A nickel based superalloy reinforced by both Ni_3Al and Ni_3V ordered-fcc precipitates

Alexander J Knowles[a,b,*], Lucy Reynolds[a], Vassili A Vorontsov[a], David Dye[a]

[a] Department of Materials, Imperial College, South Kensington, London SW7 2AZ, UK
[b] School of Metallurgy and Materials, University of Birmingham, Birmingham B15 2TT, UK

ARTICLE INFO

Article history:
Received 30 October 2018
Received in revised form 8 December 2018
Accepted 9 December 2018
Available online xxxx

Keywords:
Superalloy
Precipitation
Intermetallics
Microstructure
Mechanical properties

ABSTRACT

A nickel based superalloy has been designed where the fcc γ Ni matrix is reinforced by two different ordered-fcc intermetallic compounds, γ′ $L1_2$ Ni_3Al and γ″ $D0_{22}$ Ni_3V. Primary ageing at 900–1000 °C precipitated spherical $L1_2$ Ni_3Al, whose volume fraction and size were controlled by altering the ageing temperature and time. Secondary ageing at 700 °C for 1–1000 h precipitated $D0_{22}$ Ni_3V laths. The duplex precipitation increased hardness by up to 85 HV, with ~ 500 MPa compressive proof strength maintained at 800 °C. Electron microscopy studied the Ni_3Al precipitation and confirmed the form of the secondary Ni_3V precipitates and their long term stability.

Nickel based superalloys are widely used due to their combination of strength, creep, toughness, environmental resistance and microstructural stability in the 650–1200 °C interval [1,2]. Such alloys exploit the two-phase field that exists within the Ni-Al binary system to produce microstructures comprising a γ face-centred cubic (fcc) A1 (*Strukturbericht designation*) matrix, Fig. 1a, reinforced with γ′ $L1_2$ Ni_3Al ordered-fcc intermetallic precipitates, Fig. 1b. A variety of additional phases are used in multicomponent (~10) commercial superalloys, including other intermetallics as well as carbides and borides. However, there is an additional ordered-fcc $D0_{22}$ γ″ phase, Fig. 1c, that can be exploited in superalloys, *e.g.* Inconel 718 [3], which is also being explored in other alloy systems [4-6]. Unfortunately, the $D0_{22}$ Ni_3Nb phase in Inconel 718 is metastable [7,8] decomposing into the δ Ni_3Nb $D0_a$ orthorhombic *Pmmn* phase [9,10]. The Ni_3X type intermetallics adopt a number of stable crystal structures as the X element is changed due to differing formation energies. For Ni_3X intermetallics with X = Nb, Ta, Mo the stable structure is $D0_a$, while for X = Ti the $D0_{24}$ structure is adopted, and with X = Al and Si the traditional γ′ $L1_2$ structure is adopted [11]. The only stable $D0_{22}$ Ni_3X type intermetallic is Ni_3V [11], and notably this has not been exploited in practical alloys. The $D0_{22}$ crystal structure is of particular interest as, unlike the $D0_a$ and $D0_{24}$ structures, it is an fcc superlattice structure, being ordered across two fcc unit cells with a 3:1 A to B site ratio (Fig. 1c). Because of its distinct crystal structure, composition, lattice parameter and so misfit, $D0_{22}$ Ni_3V may exhibit a different morphology to $L1_2$ Ni_3Al as well as different coarsening kinetics and strengthening effects [12-14]. $D0_{22}$ Ni_3V has lattice parameters of a = 3.543 Å, c = 7.221 Å [15], compared to those for metastable $D0_{22}$ Ni_3Nb of a = 3.62 Å, c = 7.41 Å [7].

In this work, the $D0_{22}$ Ni_3V phase is explored. Purely on density grounds it may be of interest as the density of its unit cell is 8% lower than pure Ni, compared to 2% higher for $D0_{22}$ Ni_3Nb and 18% lower for $L1_2$ Ni_3Al. The Ni_3V phase offers some advantages over Ni_3Nb as it is thermodynamically stable and has a different lattice misfit, δ. Given $\delta = 2(a_{\gamma'} - a_{\gamma})/(a_{\gamma'} + a_{\gamma})$ and $a_{\gamma} = 3.51$ Å, $\delta a_{\gamma}\text{-}a_{Ni_3V} \sim 0.9$ %, and $\delta a_{\gamma}\text{-}c_{Ni_3V} \sim 2.8$ %, in contrast to $\delta a_{\gamma}\text{-}a_{Ni_3Nb} \sim 3.1$ %, and $\delta a_{\gamma}\text{-}c_{Ni_3Nb} \sim 5.4$ %, taking the lattice parameters given earlier for Ni_3V [15] and Ni_3Nb [7]. Further, it is possible to have controlled precipitation of $L1_2$ Ni_3Al with optimised volume fraction and size before producing $D0_{22}$ Ni_3V at a lower temperature. This is because in the Ni-Al-V ternary system the A1 Ni phase exists in equilibrium with $L1_2$ Ni_3Al at 1000 °C, Fig. 1d. However, when the temperature is lowered to 700 °C a three-phase field exists between A1 Ni, $L1_2$ Ni_3Al and $D0_{22}$ Ni_3V (Fig. 1e) [16]. This enables the $L1_2$ Ni_3Al population to be established and controlled prior to formation of $D0_{22}$ Ni_3V, Fig. 1f. A two-step heat treatment was designed to investigate the potential

* Corresponding author at: School of Metallurgy and Materials, University of Birmingham, Birmingham B15 2TT, UK.
E-mail address: a.j.knowles@bham.ac.uk (A. J Knowles).

https://doi.org/10.1016/j.scriptamat.2018.12.013
1359-6462/

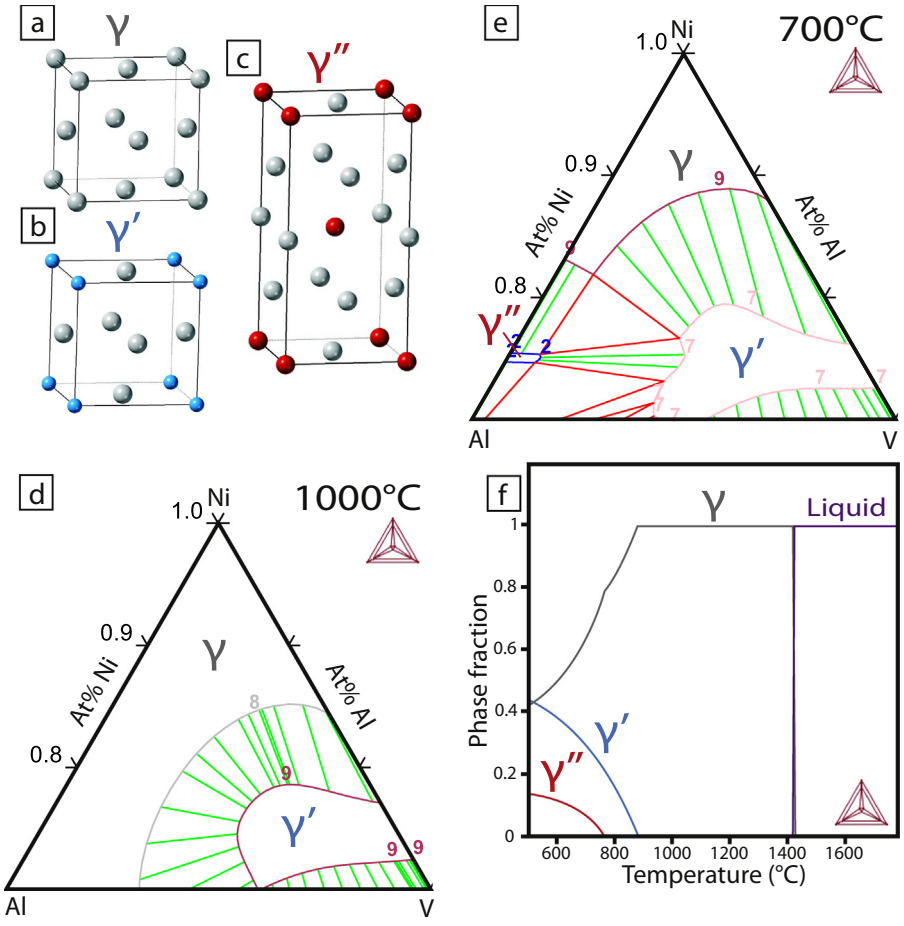

Fig. 1. Unit cells of: (a) A1 fcc γ, (b) $L1_2$ ordered-fcc γ′, (c) $D0_{22}$ ordered-fcc γ″. Al-Ni-V phase diagram isothermal sections predicted by Thermo-Calc TCNi8 at: (d) 1000 °C, (e) 700 °C. (f) Ni-14.9%V-5.2%Al (at.%) alloy predicted phase fractions vs temperature.

to form hierarchical structures of $D0_{22}$ Ni_3V within $L1_2$ Ni_3Al precipitates, as is possible in B2 and $L2_1$ ordered-bcc precipitates [17] and $L1_2$ Ni_3Al with A1 Ni precipitates [18-20].

A 300 g ingot of the Ni-14.9%V-5.2%Al (at.%) alloy was prepared by arc melting of pure (>99.9%) elements under Ar, which was used to characterise the stable phases at particular temperatures. Sections of the alloy were heat treated under protected atmosphere using evacuated quartz ampoules backfilled with argon.

The alloy was solution heat treated at 1240 °C for 24 h and water quenched. Primary ageing heat treatments were made at 1000 °C and 900 °C for 16 h to 500 h and water quenched. Secondary ageing heat treatments were made at 700 °C for 10 h to 1000 h and water quenched. Scanning electron microcopy (SEM) was performed on a Zeiss Sigma 300 operated at 5 or 10 kV for imaging and JEOL 6400 operated at 20 kV for energy-dispersive X-ray spectrometry (EDX). The bulk composition of the alloy evaluated by 200 × 400 μm EDX area measurements, was (79.0 ± 0.2)Ni– (15.6 ± 0.1)V– (5.4 ± 0.2)Al (at.%), which was considered sufficiently close to the target composition to meet the needs of the study.

The density, determined by the Archimedes method, was 8.27 g cm^{-3}. X-ray diffraction was performed to determine the phases present in the alloy using $Cu_{K\alpha}$ radiation on spun flat samples ~8 mm in diameter. Transmission electron microscopy (TEM) and scanning TEM (STEM) were performed using a JEOL 2100F microscope. TEM foils were prepared by mechanical thinning to 150 μm followed by eletropolishing using 10 vol % perchloric acid in methanol at −8 °C and 18 V. Hardness indents using a 10 kg load held for 10 s were made with the average of five measurements reported. High temperature compression tests to determine the variation in 0.2% proof strength with temperature were performed on sub-sized 2 mm cube samples that were tested at a strain rate of 10^{-3} s^{-1} under vacuum within a modified 5 kN Zwick load frame up to 800 °C [21].

The stable phases in the alloy were evaluated at a number of different times and temperatures. Homogenisation at 1240 °C for 24 h was found to be successful at removing casting-induced microsegregation and resulted in a grain size of ~300 μm (determined by the linear intercept method), see Fig. 2c. Following ageing at 1000 °C for 16 h, an area fraction of 15% spherical precipitates was attained with ~340 nm diameter, Fig. 2d. Further ageing to 200 h at 1000 °C resulted in these precipitates coarsening to ~680 nm in size. In contrast, ageing at 900 °C for 200 h resulted in a greater area fraction of 40% precipitates of ~230 nm size (Fig. 2e), which coarsened to ~350 nm after 500 h total ageing time. Secondary ageing at 700 °C was found to give a pronounced change in the microstructure of the alloy with the matrix phase found to contain a second form of precipitates produced with a lath morphology. After 100 h these exhibited a thickness of 14 ± 4 nm and a spacing of 25 ± 8 nm, Fig. 2f. Further ageing to 1000 h coarsened the lath precipitates to a thickness of 21 ± 4 nm and a spacing of 42 ± 15 nm, Fig. 2g.

X-ray diffraction was used to study the phases present in each heat treated condition, shown in Fig. 2a. In the homogenised condition, reflections consistent with single phase A1 fcc were observed. On primary ageing at 900 °C, as well as A1 reflections, additional reflections consistent with an ordered-fcc $L1_2$ phase were found indicating that the second phase present in SEM (Fig. 2e) was $L1_2$ Ni_3Al. Secondary ageing at 700 °C resulted in A1 and $L1_2$ phase reflections as well as additional reflections suggestive of a phase with the alternative ordered-fcc $D0_{22}$ structure, which were suspected to originate

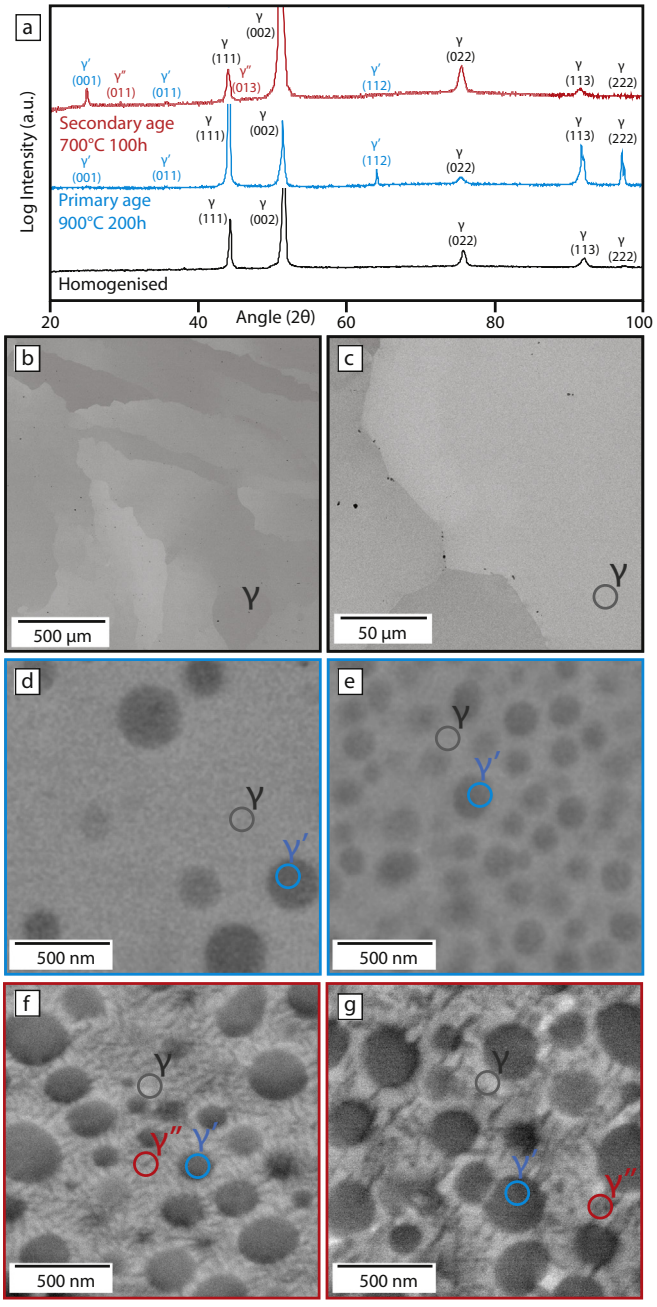

Fig. 2. Ni-V-Al alloy (a) X-ray diffraction patterns, as well as backscattered SEM micrographs of (b) as-cast, (c) homogenised at 1240 °C for 24 h, (d) primary aged at 1000 °C for 16 h, (e) primary aged at 900 °C for 200 h followed by a secondary age at 700 °C for (f) 100 h and (g) 1000 h.

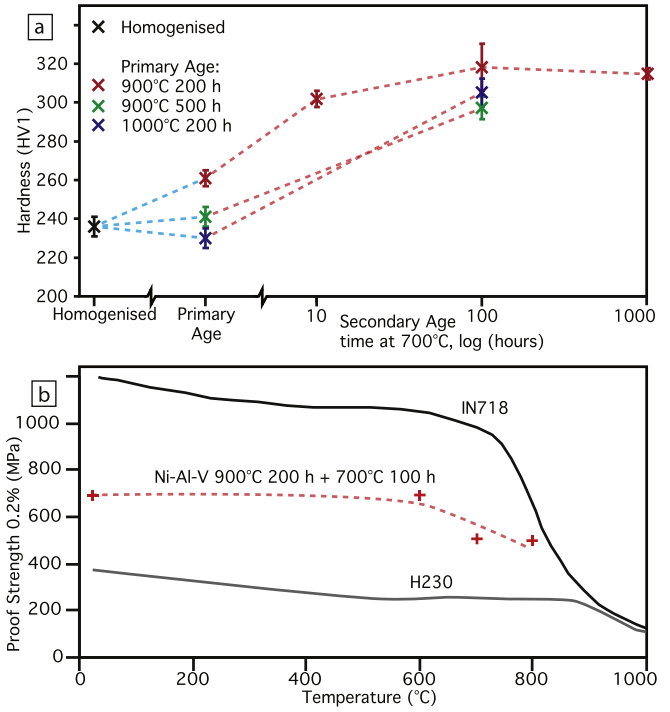

Fig. 3. Ni-Al-V alloys (a) Hardness value for the respective heat treatments and ageing curve at 700 °C, (b) 0.2% compressive proof stress plotted against IN718 and H230 tensile proof strengths, adapted from Refs. [3] and [22] respectively.

from the lath precipitates observed by SEM (Fig. 2f and g). However, the DO_{22} peaks were weak owing to the structure factor. Further study of the precipitates and the elemental segregation between phases were made by TEM and STEM as the size of the phases were below the resolution limit of SEM-EDX.

Vickers microhardness results from the alloy in each heat treated condition are shown in Fig. 3a with a 700 °C ageing curve following the 900 °C for 200 h primary age. This is plotted alongside alternative primary ages of 900 °C 500 h and 1000 °C 200 h before and after ageing at 700 °C 100 h. Of the explored primary ageing treatments, 900 °C 200 h was found to give the greatest hardness increase of ~25 HV when compared to the homogenised condition and so was selected for further secondary ageing. All primary age variants exhibited a further ageing response of ~60 HV on secondary ageing that was attributed to the laths observed by SEM (Fig. 2f and g). Long duration ageing for 1000 h found only a small hardness loss when compared to the 100 h peak hardness. Shorter ageing times are desirable from a commercial viewpoint, which could be met either by using the alloy in the underaged condition, or using a higher secondary ageing temperature where peak hardness would be anticipated after shorter times. Further work is needed to evaluate this and the overall balance of properties achieved.

High temperature compression tests were performed on the alloy after ageing at 900 °C for 200 h and then 700 °C for 100 h in order to evaluate its proof strength, Fig. 3b. For comparison, Inconel 718 [3] superalloy and Haynes 230 [22] solid solution alloy are used. While the 0.2% proof stress ($\sigma_{y,0.2}$) of 695 MPa found at room temperature was significantly lower than IN718 [3], the 800 °C $\sigma_{y,0.2}$ ~500 MPa was comparable, and the alloy out-performed H230 [22] at all temperatures evaluated. These findings for the simple ternary alloy are promising when compared to complex commercialised alloys with their many additions and optimisation iterations. Superalloys are typically exposed to oxidising conditions at high temperature and so it is important for their oxidation resistance to be evaluated. Thermogravimetric analysis (TGA) of the alloy, primary aged at 900 °C for 200 h and secondary aged at 700 °C for 100 h, was performed at 700 °C for 24 h in air found parabolic oxidation kinetics, with a power law ($y = x^n$) exponent of $n = 0.52$, see Supplementary Fig. 2. However, this was markedly faster than that reported for IN718 [23] after 24 h, which was attributed to the lower Al and Cr contents in the simple ternary alloy.

Scanning transmission electron microscopy (STEM) was performed to study the secondary precipitates in greater detail on a coarsened sample that was primary aged at 900 °C for 200 h and then long duration secondary aged at 700 °C for 1000 h. TEM and STEM analysis was also performed after 100 h, see Supplementary information. In this condition, SADPs were obtained from purely the spherical $L1_2$ Ni_3Al precipitates (Fig. 4a), as well as from both spherical and lath precipitates (Fig. 4b). STEM annular dark field (ADF)

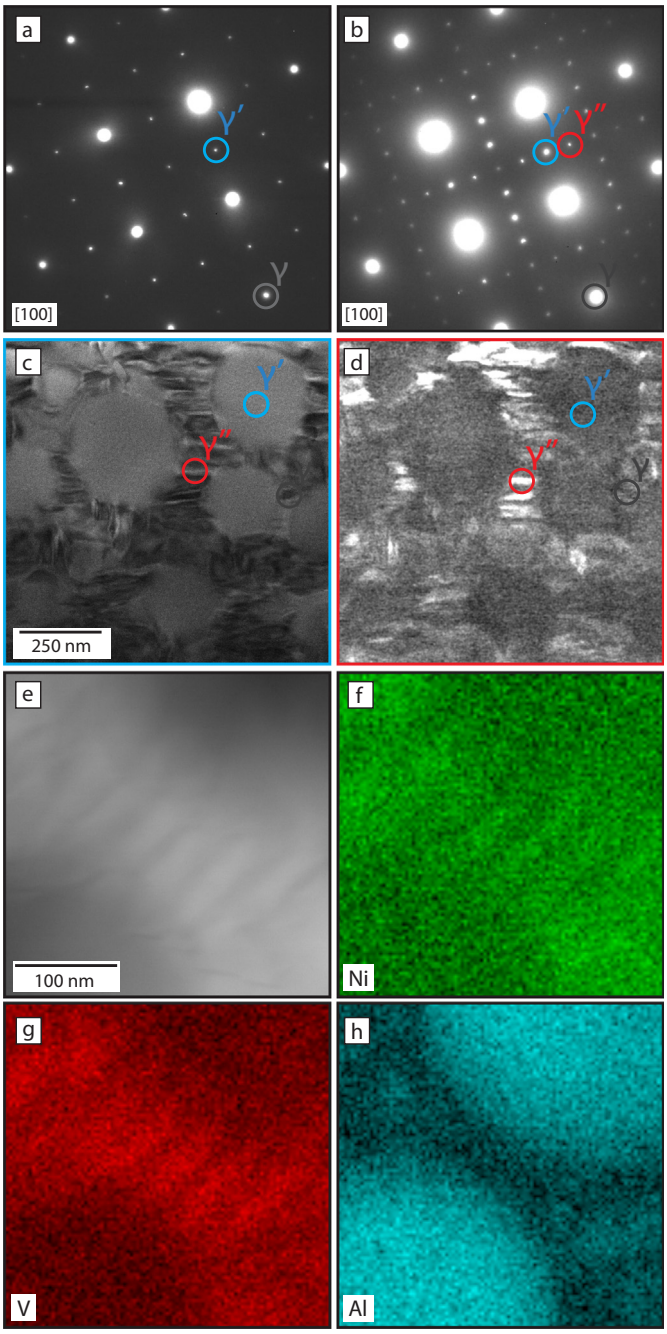

Fig. 4. Alloy following secondary ageing at 700 °C for 1000 h: (a) SAPD from a spherical $L1_2$ Ni_3Al precipitate, (b) SAPD from matrix and both spherical and lath precipitates, (c) STEM-ADF with aperture around blue circled reflection, (d) STEM-ADF with aperture around red circled reflection. (e) STEM-HAADF, with STEM-EDX maps for (f) Ni, (g) V and (h) Al. (For interpretation of the references to color in this figure legend, the reader is referred to the web version of this article.)

imaging was then used and by carefully positioning the objective aperture it was possible to not only highlight the $L1_2$ precipitates (Fig. 4c) but also to separate and image using solely the $D0_{22}$ superlattice reflections (Fig. 4d). The latter were found to correspond to the lath precipitates, confirming that they were $D0_{22}$ structured. STEM-EDX mapping of the sample (Fig. 4 e–h) found Al segregation to the $L1_2$ precipitates consistent with Ni_3Al. It was also found that the coarsened laths were rich in V consistent with them being Ni_3V, where the equal aluminium concentration between A1 Ni and $D0_{22}$ Ni_3V matches the phase diagram (Fig. 1b). While richer in V, it was found that a significant quantity of V was dissolved within the $L1_2$ Ni_3Al. This is in agreement with the marked ternary solubility for V in Ni_3Al within the Ni-Al-V ternary phase diagram (Fig. 1a and b).

It was suspected that the solubility for V within $L1_2$ Ni_3Al may decrease with temperature in a similar manner to that for hierarchical structured ferritic superalloys. In these alloys the Fe rich A2 matrix contains 60–200 nm B2 NiAl precipitates from within which 15–20 nm $L2_1$ precipitates nucleate and grow within the B2 precipitates [17]. This is similar to the precipitation of A1 Ni from within $L1_2$ Ni_3Al [18-20] owing to the decreased solubility for Ni within Ni_3Al with temperature. If the solubility for V within Ni_3Al changed with temperature this would enable the precipitation of $D0_{22}$ Ni_3V from within $L1_2$ Ni_3Al. However, no precipitation within the $L1_2$ Ni_3Al was observed, with the $D0_{22}$ Ni_3V only found within the A1 Ni matrix instead. This indicated that there is minimal change in V solubility within $L1_2$ Ni_3Al from 900 °C to 700 °C.

In summary, the following conclusions can be drawn.

(1) A new nickel based superalloy has been designed and produced that comprises two ordered-fcc precipitates, γ' $L1_2$ and γ'' $D0_{22}$. Such precipitation has been demonstrated for Ni_3Nb in Inconel 718 and other alloys, however, Ni_3Nb is metastable in the $D0_{22}$ structure. In contrast, the stable $D0_{22}$ structured Ni_3V intermetallic observed here has not been explored as a superalloy reinforcing phase.

(2) A peak primary age of 900 °C for 200 h was determined where 40% area fraction of ~230 nm spherical γ' $L1_2$ Ni_3Al precipitates were produced, giving 25 HV hardening. No $D0_{22}$ precipitated at this temperature allowing the γ' formation to be controlled and optimised.

(3) Secondary ageing at 700 °C for 100 h formed fine laths with a thickness of 14 ± 4 nm and a spacing of 25 ± 8 nm, which gave nearly 60 HV of additional hardness. These lath precipitates were determined by TEM to be $D0_{22}$ Ni_3V with chemical segregation consistent with the Ni-Al-V phase diagram. No formation of $D0_{22}$ Ni_3V within the previously formed $L1_2$ Ni_3Al precipitates was observed, indicating that the solubility for V within $L1_2$ Ni_3Al does not change markedly from 900 to 700 °C.

Acknowledgments

R Dodds and I Bantounas assisted with the alloy production, while S A Humphrey-Baker assisted with thermogravimetric analysis. Support is acknowledged: by A J Knowles for an Engineering and Physical Sciences Research Council Doctoral Prize Fellowship (EP/N509486/1) and, with D Dye, the Engineering and Physical Sciences Research Council "DARE" grant (EP/L025213/1), as well as by V A Vorontsov an Imperial College London Junior Research Fellowship.

Appendix A. Supplementary data

Supplementary data to this article can be found online at https://doi.org/10.1016/j.scriptamat.2018.12.013.

References

[1] M.J. Donachie, S.J. Donachie, Superalloys: A Technical Guide, 2nd ed., ASM Int. 2002.
[2] R. Reed, The Superalloys: Fundamentals and Applications, CUP. 2006.
[3] Special Metals, Inconel® Alloy 718 Datasheet, SMC-045. 2007, 1–28.
[4] P.M. Mignanelli, N.G. Jones, E.J. Pickering, O.M.D.M. Messe, C.M.F. Rae, M.C. Hardie, H.J. Stone, Scr. Mater. 136 (2017) 136–140.
[5] X. Gao, R. Hu, G. Luo, Scr. Mater. 134 (2017) 15–19.
[6] I.J. Moore, M.G. Burke, E.J. Palmiere, Acta Mater. 119 (2016) 157–166.
[7] A. Kaufman, N.J. Hoffmann, H. Lipson, Scr. Metall. 3 (1969) 715–720.
[8] Y. Du, Y.A. Chang, W. Gong, B. Huang, H. Xu, Z. Jin, F. Zhang, S.L. Chen, Intermetallics 11 (2003) 995–1013.

[9] D. Srinivasan, Mater. Sci. Eng. A 364 (2004) 27–34.
[10] R. Krakow, D.N. Johnstone, A.S. Eggeman, D. Hünert, M.C. Hardy, C.M.F. Rae, P.A. Midgley, Acta Mater. 130 (2017) 271–280.
[11] H. Sugimura, Y. Kaneno, T. Takasugi, Mater. Trans. 52 (2011) 663–671.
[12] J.M. Oblak, D.F. Paulonis, D.S. Duvall, Metall. Trans. 5 (1974) 143–153.
[13] D.C. Lv, D. McAllister, M.J. Mills, Y. Wang, Acta Mater. 118 (2016) 350–361.
[14] Y. Zhao, L. Qi, Y. Jin, K. Wang, J. Tian, P. Han, J. Alloys Compd. 647 (2015) 1104–1110.
[15] J. Mass, G. Bastin, F. Loo, R. Metselaar, Z. Met. 74 (1983) 294–299.
[16] H. Zapolsky, C. Pareige, L. Marteau, D. Blavette, Calphad 25 (2001) 125–134.
[17] C.H. Liebscher, V.R. Radmilović, U. Dahmen, N.Q. Vo, Acta Mater. 92 (2015) 220–232.
[18] A.J. Ardell, M. Pozuelo, Intermetallics 88 (2017) 81–90.
[19] Y. Ma, A.J. Ardell, Acta Mater. 55 (2007) 4419–4427.
[20] W.H. Tian, T. Sano, M. Nemoto, Scr. Metall. 20 (1986) 1–4.
[21] T.P. Chapman, K.M. Kareh, M. Knop, T. Connolley, P.D. Lee, M.A. Azeem, D. Rugg, T.C. Lindley, D. Dye, Acta Mater. 99 (2015) 49–62.
[22] Haynes International, Haynes® 230® Alloy Datasheet H-3000 M, 2018, 1–28.
[23] G.A. Greene, C.C. Finfrock, Oxid. Met. 55 (2001) 505–521.